JMEPEG (2022) 31:10089–10098
https://doi.org/10.1007/s11665-022-06990-3

1059-9495/$19.00

TECHNICAL ARTICLE

As-Cast High Entropy Shape Memory Alloys of $(TiHfX)_{50}(NiCu)_{50}$ with Large Recoverable Strain and Good Mechanical Properties

Guangwei Zhao, Da Li, Guoxiong Xu, Dong Fang, Yongsheng Ye, Caihua Huang, and Zengmin Shi

Submitted: 13 December 2021 / Revised: 6 April 2022 / Accepted: 25 April 2022 / Published online: 11 May 2022

The proposal of a high entropy shape memory alloy (HESMA) has opened a new field for the application of high-entropy alloys (HEAs) and the development of shape memory alloys (SMAs). However, to date, the recoverable strains of reported HESMAs have been generally modest, and their preparation processes have been complex. In this work, novel as-cast $(TiHfX)_{50}(NiCu)_{50}$ HESMAs with a very large recoverable strain (9.4%) and excellent mechanical properties were fabricated. A lower elastic modulus and lattice distortion strengthening effect were considered to contribute to the large recoverable strain characteristics of HESMAs. The strategy of finding HESMAs with good comprehensive properties by designing low C_v values may provide useful guidelines in this field.

Keywords high entropy alloys, martensitic phase transformation, mechanical properties, shape memory alloys, superelasticity

1. Introduction

Recently, Firstov et al. (Ref 1) proposed the concept of a high-entropy shape memory alloy (HESMA), which combines a high-entropy alloy (HEA) (Ref 2-4) with a shape memory alloy (SMA) for the first time. This work has opened a new field for the application of HEAs and the development of SMAs. An HESMA exhibits the properties of an HEA and an SMA at the same time. Therefore, it can be used as a structural material, functional material, or both. This material may have potential applications in many fields, such as aerospace, machinery, automotive, electronics, petroleum engineering, civil engineering and biomedicine. The first reported TiZrHfCoNiCu HESMA could completely recover 1.63% prestrain in the cast state (Ref 1, 5, 6) and 3-5% after heat treatment due to sufficient martensite transformation (MT) of the uniform microstructure (Ref 7, 8). Subsequently, Chen (Ref 9) and Chang (Ref 10) et al. designed a $(TiZrHf)_{50}(NiCu)_{50}$ HESMA with a much higher MT temperature. Li et al. (Ref 11, 12) fabricated two HESMAs, $Ti_{20}Zr_{15}Hf_{15}Ni_{25}Cu_{25}$ and $Ti_{25}Zr_{10}Hf_{15}Ni_{25}Cu_{25}$, which could fully recover 4% prestrain in 185-285 °C. Moreover, Canadinc et al. (Ref 13) reported a TiZrHfNiPd HESMA and achieved ultrahigh phase transformation temperatures. Piorunek et al. (Ref 14, 15) reported a TiZrHfNiCuPd HESMA and found that the MT temperature increased with a composition deviation parameter. In addition, some β-Ti-type HESMAs have also been reported, such as TiZrHfAlNb (Ref 16), TiZrHfNbTaSn (Ref 17), and TiZrHfNbTaAl (Ref 18), which can realize stress-induced MT by the $\beta \rightarrow \alpha''$ transformation.

The above research progress is valuable because it enables the development of new HESMAs. However, further research is still needed in the following areas. First, compared with traditional TiNi-based SMAs, the recoverable strains of reported HESMAs (generally approximately 3-5%) can be substantially improved. Second, most reported HESMAs need to undergo complex preparation processes, such as long-term heat treatment (Ref 9, 14, 15, 19) or plastic deformation (Ref 16-18). Third, some researchers have reported HESMAs are too costly due to the addition of Pd. Fourth, the compositions of the reported HESMAs have been limited to the early definition of HEA; that is, the mixing entropy is higher than 1.5R, or each element is between 5 and 35 at. % (Ref 2, 3). However, due to the rapid development of HEA, its definition has been continuously expanded, such as the recently reported HESMAs of $Cu_5Ni_{45}Hf_{16.67}Ti_{16.67}Zr_{16.67}$ (Ref 10), $Ni_{50}Hf_{16.67}Ti_{16.67}Zr_{16.67}$ (Ref 10), $Ti_{50}Zr_{20}Hf_{15}Al_{10}Nb_5$ (Ref 16), $Ti_{49}Zr_{20}Hf_{15}Al_{10}Nb_6$ (Ref 16), $(TiZrHf)_{87}Nb_5Ta_5Al_3$ (Ref 18), $Ti_{40}Zr_{10}Ni_{40}Co_5Cu_5$ (Ref 3, 19), $Ti_{38}Zr_{25}Hf_{25}Ta_{10}Sn_2$ (Ref 20), and $Ti_{38}Zr_{25}Hf_{25}Ta_7Sn_5$ (Ref 20), and the eutectic HEAs of $Fe_{55}Cr_{15}Ni_{(30-x)}Nb_x$ (Ref 4), which are not within the limits of the above definition but exhibit the good properties of HEAs. Therefore, the purpose of this work is to develop HESMAs with highly recoverable strain and a composition that is not limited to the traditional definition of an HEA using a low-cost, simple preparation process. Eight alloy elements, Ti, Ni, Hf, Cu, Y, Nb, Zr, and Cr, were selected and divided into two categories: A=(Ti, Hf, X) and B=(Ni, Cu), where elements X is Y, Zr, Nb, and Cr. The atomic ratio of A and B was kept equal according to Firstvo's method (Ref 1, 6), i.e., $A_{50}B_{50}$, but each

Guangwei Zhao, Dong Fang, Yongsheng Ye, and **Caihua Huang**, Hubei Engineering Research Center for Graphite Additive Manufacturing Technology and Equipment, China Three Gorges University, Yichang 443002, China; and College of Mechanical and Power Engineering, China Three Gorges University, Yichang 443002, China; and **Da Li, Guoxiong Xu,** and **Zengmin Shi**, College of Mechanical and Power Engineering, China Three Gorges University, Yichang 443002, China. Contact e-mail: zgwhit@163.com.

element was not limited to 5-35% in this work. The original intent of this composition design was that Hf and Ni had good solubility and similar electronic configuration in Ti and Cu, respectively, so that they could replace each other when forming HESMAs (Ref 10). Moreover, the selected X elements are inexpensive and have been commonly used to improve strength, plasticity and memory properties in many HEAs and SMAs (Ref 2, 10, 11, 16-19, 22).

2. Experimental Procedure

The as-cast $(TiHfX)_{50}(NiCu)_{50}$ (at. %) ingots with a nominal composition of $Ti_{35}Hf_{10}X_5Ni_{44}Cu_6$ (X = Y, Zr, Nb, Cr) were prepared by vacuum arc melting using high-purity raw materials under an argon atmosphere (hereafter, the four alloys are referred to as Y5, Zr5, Nb5 and Cr5 for convenience). Each sample was remelted six times and held in liquid state for at least two minutes in each melting cycle to ensure homogeneity. The phase structure was analyzed by x-ray diffraction (XRD, EDX-7000) at a rate of 4°/min. The microstructure features were characterized by using scanning electron microscopy (SEM, JEOL/JSM-7500F) equipped with energy dispersive x-ray spectroscopy (EDX, Bruker/X-Flash). The transformation behaviors were investigated using differential scanning calorimetry (DSC, STA-449-F5) at a heating and cooling rate of 15 °C/min. The mechanical and superelasticity (SE) properties were tested on a universal electronic testing machine (WDW-100A) with a strain rate of 0.001 s^{-1} (0.36 mm/min) and the dimensions of the cylindrical samples were $\varphi 3 \times 6$ mm.

3. Results and Discussion

3.1 Microstructure and Transform Behavior

Figure 1(a) shows that the Mp (peak temperature of the MT) for Zr5 and Y5 are approximately − 20 and − 26 °C, respectively, but there are no obvious peaks for Cr5 and Nb5 during cooling. The Ap (peak temperature of the austenite transformation) for Zr5 and Nb5 are approximately 10 and 45 °C, and two endothermic peaks at 38 and 76 °C are detected for Y5, but no obvious peak for is detected again. The phase transition peaks of some alloys are not detected, which may be because there is no thermally-induced martensitic transformation in this temperature range (Ref 16, 19), or the phase transition temperature is lower than the minimum detection temperature of the equipment (Ref 22). Figure 1(b) shows that the four HESMAs mainly consist of B2 austenite and a few compounds. This is consistent with the empirical results that HEAs with highly negative ΔH values (enthalpies of mixing) and relatively large δ (atomic size difference) (Table 1) values (Table 1) usually cannot form a single-phase solid solution (Ref 9). The main diffraction peaks can be indexed as (100), (110), (200), (210), (211) and (220) (Ref 21-24). Compared with the reported ternary or quaternary Ti-Ni-Cu-based SMAs (Ref 21, 22, 25-27), some of the diffraction peaks obviously shifted, which may be caused by the severe lattice distortion effect in the HEAs (Ref 1, 5, 9). All four HESMAs have obvious dendrite microstructures, and a few compounds are distributed among the dendrites. The element mapping results (Fig. 1c-f) show that the dark gray phase in Y5 is a Y-Cu compound, the gray phase in Nb5 is a Nb-rich phase and contains a small amount of martensite, the white phase in Zr5 is rich in Hf and Zr, and the light gray compound in Cr5 is rich in Cr. Although the compounds may have some influence on the performance of HESMAs, due to their small number, it is believed that the matrix structure should be the most important factor.

3.2 Mechanical and Superelasticity Properties

Figure 2 shows the compression curves of the four as-cast HESMAs. The results of Y5 and Zr5 show a typical double yield shape of a superelastic alloy, and the compression strength and fracture strain are 2115 MPa and 30.94% and 2498 MPa and 33.41%, respectively. However, the corresponding results of Cr5 and Nb5 are only approximately 2177 MPa and 7.0% and 2060 MPa and 8.7%, respectively. Figure 3 shows the morphology of the compression fracture surfaces of the Y5 (a), Zr5 (b), Nb5 (c) and Cr5 (d) as-cast HESMAs. All the alloys show a mixed morphology of cleavage fracture and ductile fracture. According to the compression curve, the stress of Y5 and Zr5 increases slowly in the compression process due to the lower elastic modulus of the alloys. The compression energy results from the processes of austenite elastic deformation, stress-induced martensitic transformation, redirection and elastic deformation of the stress-induced martensite, and comprehensive deformation of martensite (Ref 21, 22). Therefore, Y5 and Zr5 show good plasticity. However, the compressive stress of Nb5 and Cr5 reaches the fracture strength rapidly because of the higher elastic modulus, so the fracture strain is low. In addition, more cracks and tear steps are found on the fracture surfaces of Nb5 and Cr5, which may also be the cause of poor plasticity. Figure 4(a)-(d) shows the loading–unloading curves with increased prestrain from 2 to 15%. The stress step size is 2% for the first five cycles and 1% for the last five cycles. Figure 4(a) shows the typical loading–unloading stress–strain curve of the $(TiHfX)_{50}(NiCu)_{50}$ alloy, in which ε_r is the recoverable strain, ε_{SE} is the superelastic recovery rate, ε_E is the elastic recovery rate, ε_i is the residual strain, ε_{Pre} is the prestrain of loading, and η is the shape recovery rate. The corresponding relationship between the parameters is $\varepsilon_{Pre} = \varepsilon_r + \varepsilon_i$; $\varepsilon_r = \varepsilon_{SE} + \varepsilon_E$; $\eta = \varepsilon_r/\varepsilon_{Pre}$. This calculation method is often used for recoverable strain measurements (Ref 16-18, 21, 22, 28, 29). With increasing prestrain, the recoverable strain (ε_r) and residual strain (ε_i) increase continuously (Fig. 4e), and the shape recovery rate (η) first increases rapidly and then tends to be stable or decrease slowly (Fig. 4f). Taking Zr5 as an example, ε_r and ε_i increase from 1.00 to 8.81 and 1.00 to 6.23%, respectively, and η increases rapidly from 50 to 95% and then decreases slowly to 90%. In this process, the recoverable elastic strain (ε_E) increases from 0.6 to 3.96% (Fig. 4g), while the SE strain (ε_{SE}) increases from 0.40 to 4.95% and gradually decreases to 4.81% (Fig. 4h). There may be two different mechanisms for the variation trends of the above parameters. First, for Cr5 and Nb5, elastic recovery is dominant during the cycle, and its rate of increase is higher than that of SE recovery. Moreover, a small increase in residual strain (Fig. 4e) means less plastic deformation before fracture. Therefore, η changes little after the second cycle until fracture. Second, SE recovery is dominant for Zr5 and Y5. Compared with Zr5, the SE recovery of Y5 increases more slowly, resulting in a short decrease in η after two compression cycles (Fig. 4f). In addition, there may be two possible reasons for the slight

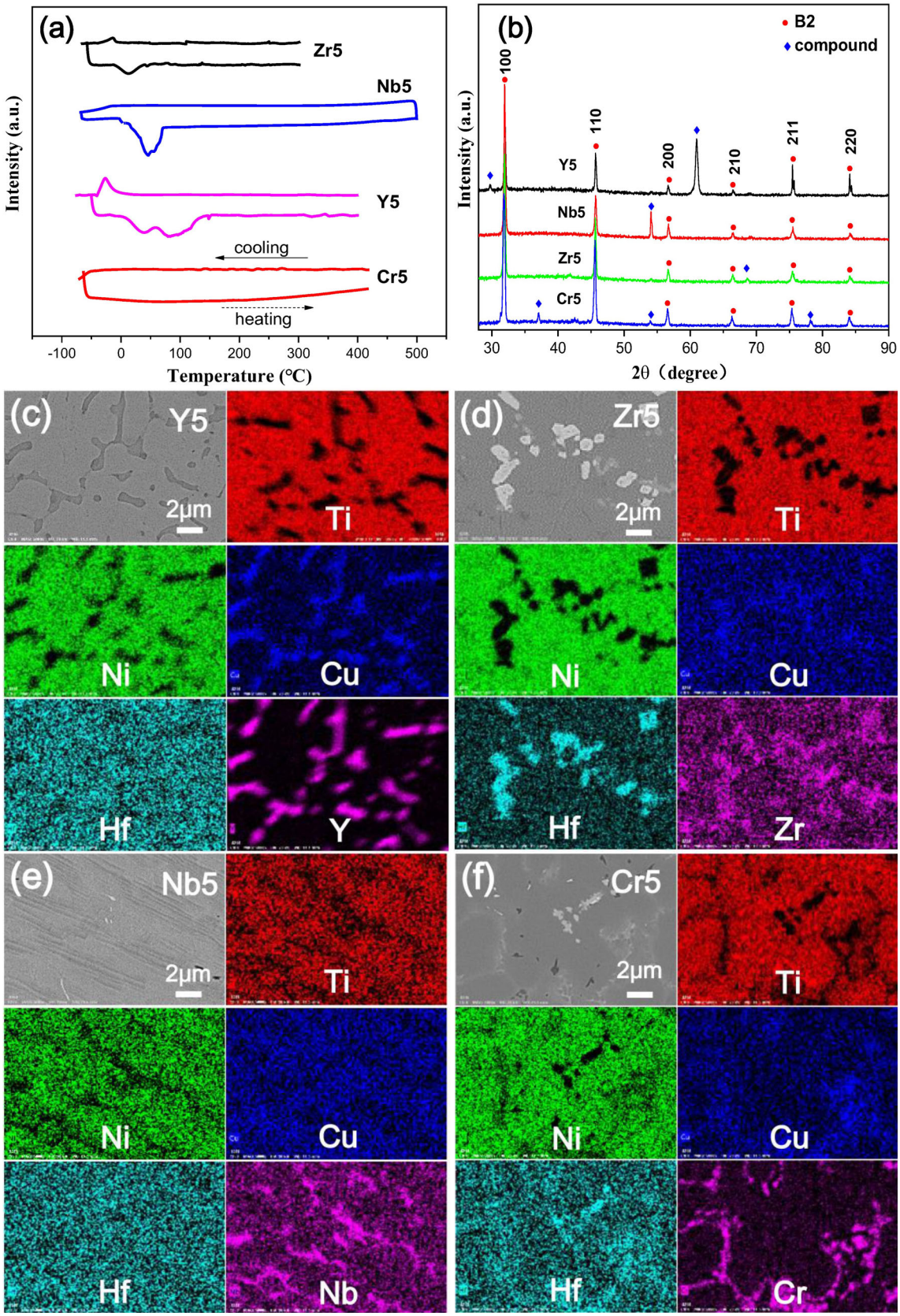

Fig. 1 The DSC curves (a), XRD patterns (b) and EDS element mapping results of Y5 (c), Zr5 (d), Nb5 (e) and Cr5 (f) as-cast HESMAs

decrease in η after reaching the maximum value. On the one hand, with increasing prestrain, plastic deformation and residual strain gradually increase, so η decreases (Ref 28-30). On the other hand, plastic deformation and dislocation have an inhibition effect on the reverse MT (Ref 31), which may produce residual martensite after unloading.

Table 1 Values of ΔH, δ, e_v/a and C_v of the investigated $(TiHfX)_{50}(NiCu)_{50}$ HESMAs

Alloys	ΔH (KJ/mol)	δ (%)	e_v/a	C_v
Y5	− 31.42	10.96	7.01	0.226
Zr5	− 34.28	9.39	7.06	0.228
Nb5	− 32.08	8.81	7.11	0.229
Cr5	− 30.84	8.82	7.16	0.233
Al5	− 34.52	8.88	7.01	0.236
V5	− 31.40	8.73	7.11	0.236
Mn5	− 31.15	8.88	7.21	0.239
Co5	− 32.28	8.91	7.31	0.241
Ta5	− 32.23	8.81	7.11	0.218

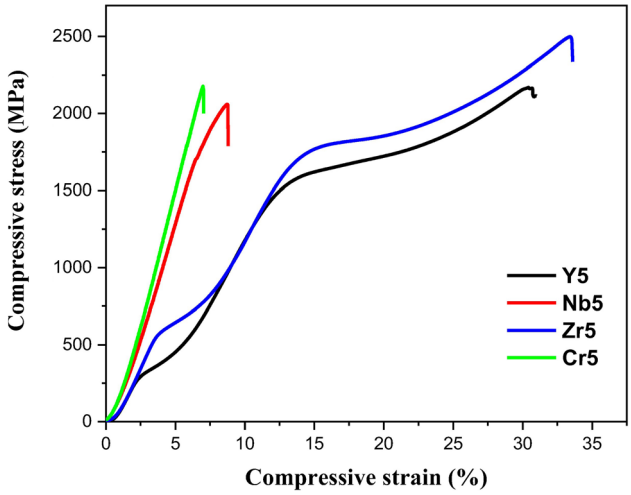

Fig. 2 The compression stress-strain curves of the $(TiHfX)_{50}(NiCu)_{50}$ HESMAs

Figure 5(a)-(c) shows the cyclic compression curves of Y5, Zr5 and Nb5 with a fixed prestrain of 6% (Cr5 fractured in the second cycle and is not shown here). The results show that the maximum compression stress increases with the number of compression cycles, and ε_i decreases rapidly to zero and finally reaches an equilibrium state with ε_E and ε_{SE} (Fig. 5d-f)). This is mainly caused by the work hardening effect of high-density dislocations accumulating at/near the interface of austenite and the stress-induced martensite in the cycle compression processes (Ref 32, 33). In addition, the participation of residual martensite in the deformation process may be another reason for the increase in maximum stress. However, as the occurrence of stress-induced martensite tends to proceed along its habitual plane (Ref 34, 35) and the volume fraction of martensite variants with favorable orientation gradually increases (Ref 28), the generation of new dislocations will gradually decrease. Then, the amount of stress-induced martensite tends to stabilize, and the change in the maximum compression stress, elastic strain and SE recovery strain gradually decrease. In fact, the increase in maximum stress will lead to plastic deformation (Ref 21, 22). However, the high strength of the HESMA ensures that this does not happen and at the same time ensures the good cycle stability of HESMA. When compared with the reported HESMAs and SMAs (Ref 2, 5-9, 12, 15, 16, 19, 21, 22, 24, 36-46) shown in Fig. 6, the HESMAs in this work show an excellent combination of maximum recoverable strain (ε_{Mr}) and high strength (σ_M, stress at maximum recoverable strain). Although the σ_M-values of TiNiCuZrSi (Ref 24) and TiNiHfNb (Ref 36) are close to those of HESMAs, their ε_{Mr} values are less than that of Zr5. In addition, their preparation processes have undergone homogenization, solution treatment, quenching and so on. Only the (TiNiHf+B_4C) composite SMAs (Ref 40) have slightly larger ε_{Mr} and σ_M values than the Zr5 HESMAs. However, compared with as-cast HESMAs, this composite material was prepared by the hot-pressed sintering (HPS)

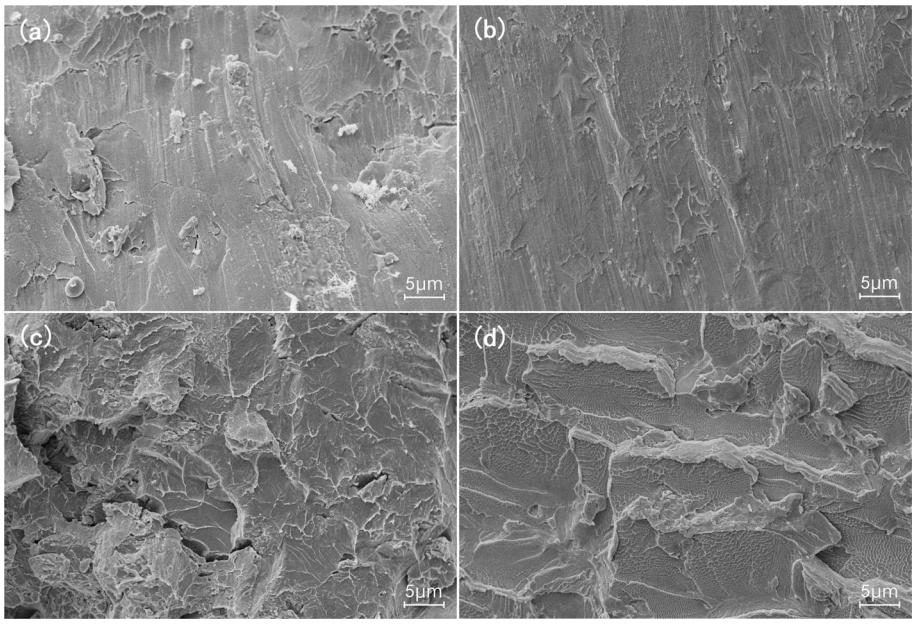

Fig. 3 The morphology of compression fracture surfaces of the Y5 (a), Zr5 (b), Nb5 (c) and Cr5 (d) as-cast HESMAs

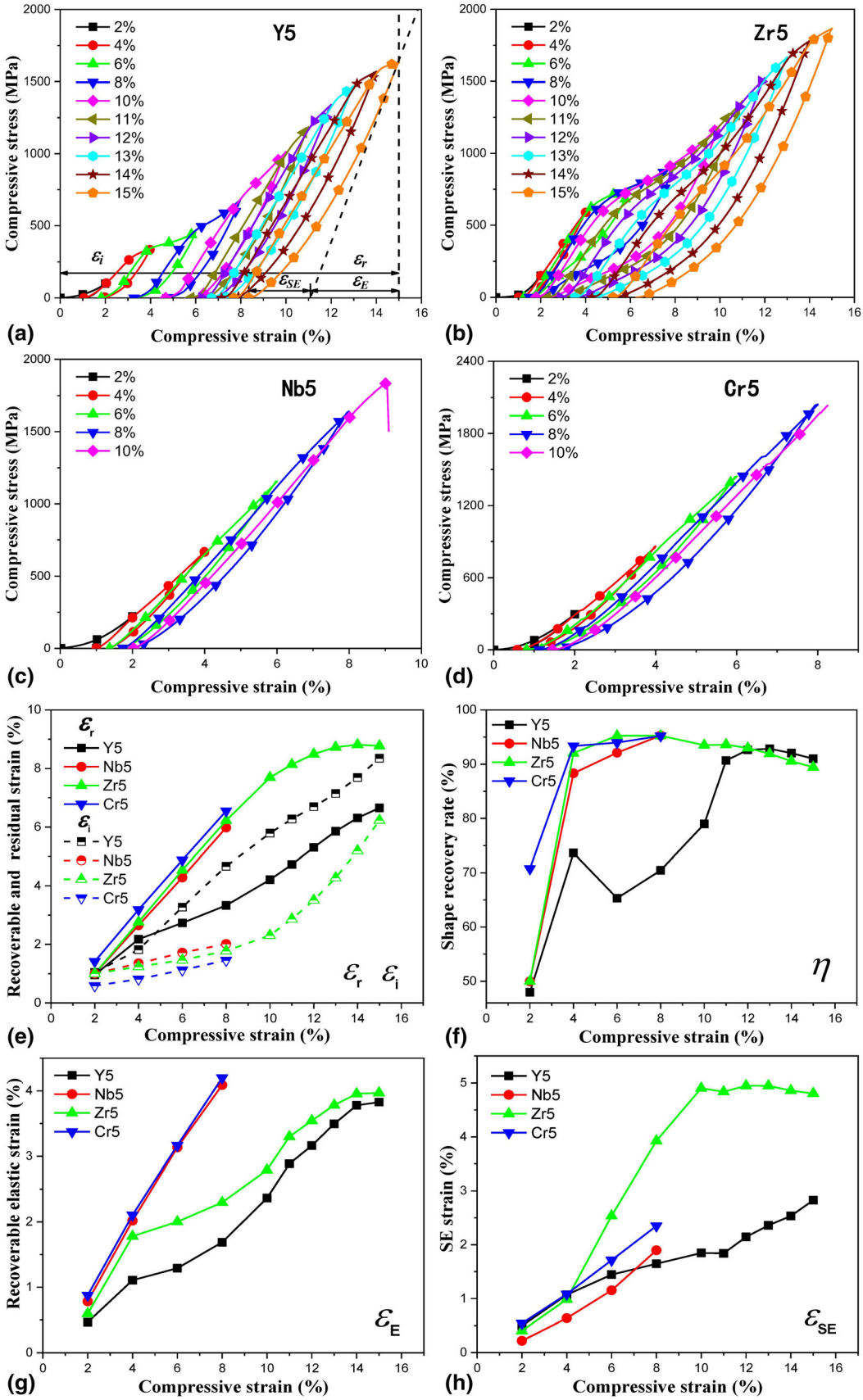

Fig. 4 Loading-unloading curves of Y5 (a), Zr5 (b), Nb5 (c) and Cr5 (d) HESMAs; the evolution of recoverable and residual strain (e), shape recovery rate (f), recoverable elastic strain (g) and SE strain (h) for the cyclic loading results

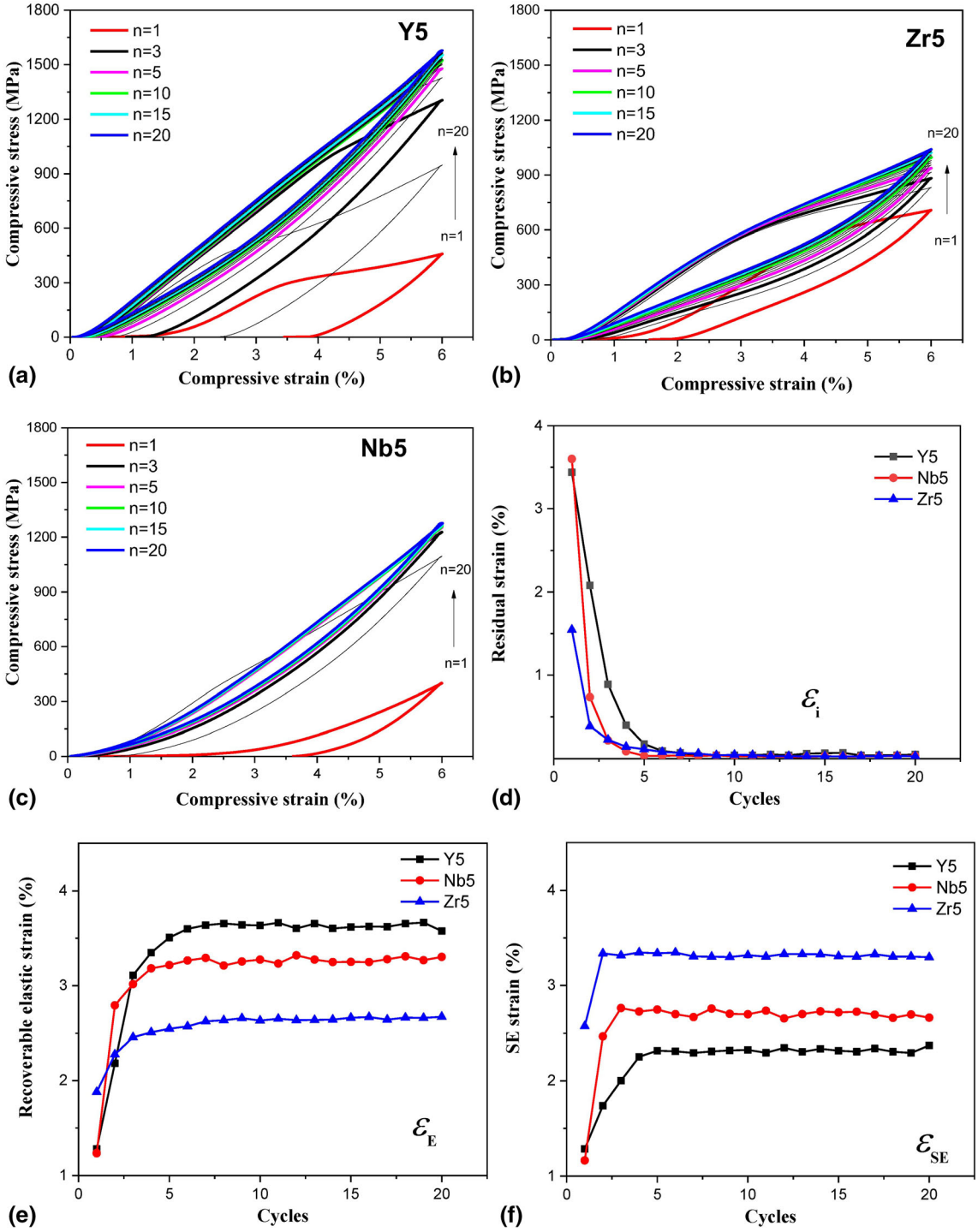

Fig. 5 The loading-unloading curves with fixed prestrain of Y5 (a), Zr5 (b) and Nb5 (c) HESMAs; the evolution of residual strain (d), recoverable elastic strain (e) and SE strain (f) for the cyclic loading results

method, which is more complex and costly. In addition, the fracture strain of this composite was only 15% (Ref 40), which is less than 50% of the Zr5 HESMAs in this work.

The above results and analysis indicated that the 5% X component had important influences on the performance of the as-cast HESMAs. Although it is difficult to comprehensively understand all the mechanisms affecting the properties of HESMAs, some relationships can be discussed here because the difference between the four HESMAs is only the 5% X component. As shown in Table 1, Zr5 and Y5 have smaller e_v/a (average valence electrons per atom, and $e_v/a=f_{Ti}\,e_v^{Ti}+f_{Hf}\,e_v^{Hf}+f_X\,e_v^X+f_{Ni}\,e_v^{Ni}+f_{Cu}\,e_v^{Cu}$, f_{Ti}, f_{Hf}, f_X, f_{Ni}, and f_{Cu} represent the atomic fraction of Ti, Hf, X, Ni and Cu atom in $(TiHfX)_{50}(Ni\text{-}Cu)_{50}$ alloy, respectively, e_v^{Ti}, e_v^{Hf}, e_v^X, e_v^{Ni} and e_v^{Cu} represent the

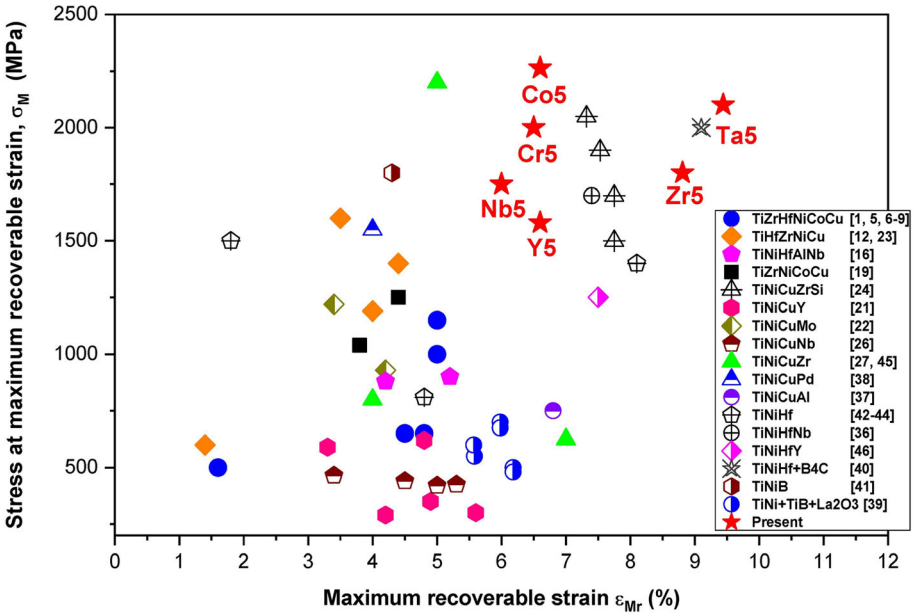

Fig. 6 The comparison map of maximum recovery strain and the corresponding stress including various Ti-based superelastic alloys and the present HESMAs

number of valence electrons of Ti, Hf, X, Ni and Cu atom) and C_v (valence electron concentration, $C_v=\left(f_{Ti}e_v^{Ti}+f_{Hf}e_v^{Hf}+f_Xe_v^X+f_{Ni}e_v^{Ni}+f_{Cu}e_v^{Cu}\right)/f_{Ti}Z^{Ti}+f_{Hf}Z^{Hf}+f_XZ^X+f_{Ni}Z^{Ni}+f_{Cu}Z^{Cu}$, Z^{Ti}, Z^{Hf}, Z^X, Z^{Ni} and Z^{Cu} represent the number of outermost electrons of Ti, Hf, X, Ni and Cu atom) values than Nb5 and Cr5. In general, the trend of VED (valence electron densities) in both austenite and martensite is similar to C_v; that is, alloys with lower C_v values show lower VEDs (Ref 47). It is known that lower VEDs of TiNi-based SMAs are expected to result in lower bulk, shear and elastic moduli (Ref 47-49). Due to the high elastic modulus or strong resistance to elastic deformation, the compression stresses of Nb5 and Cr5 increase much more rapidly (1800-2000 MPa at 8% strain) than Zr5 and Y5 (600-800 MPa at 8% strain). When they exceed the fracture stress, Nb5 and Cr5 will fracture without obvious stress-induced MT. Zr5 and Y5 can complete the transformation before fracture due to a lower elastic modulus, showing better mechanical and SE properties. Compared with Y, Zr has a higher solubility, similar atomic radius and similar electronic configuration in Ti-Ni-Cu-Hf-based SMAs (Ref 1, 10). Then, Zr tends to form a solid solution and exerts the strengthening role of lattice distortion in the HEA. Therefore, Zr5 has better comprehensive properties than Y5. Moreover, Y-rich compounds tend to form among the dendrites, which may cause the performance of Y5 to decrease (Ref 21). In addition, it is found that the strain hysteresis of Zr5 and Y5 is higher than that of Cr5 and Nb5. This may be caused by their higher values of δ_r (Table 1) because it is possible that a greater atomic size of the alloying elements results in more energy dissipation (Ref 47).

3.3 Influence of Cv on the Superelasticity Properties

Based on the above analysis, it was found that HESMAs with smaller C_v values probably have the potential for good comprehensive properties. To prove this hypothesis, five other $(TiHfX)_{50}(NiCu)_{50}$ HESMAs were prepared through the same process. The X-components were Co, Al, V, Mn and Ta, which are often used in HEAs (Ref 2-4) and SMAs (Ref 50). Compared with Y5, Zr5, Cr5, and Nb5, the newly prepared Co5, Al5, V5, and Mn5 had larger C_v values, and Ta5 had a smaller C_v (Table 1). Figure 7 shows the cycle compression results of the newly prepared HESMAs. The Co5, Al5, V5, and Mn5 HESMAs fractured during the 4-5th cycle of compression. Their maximum recoverable strains and the corresponding compression stress were 6.44% and 2263 MPa, 4.7% and 1653 MPa, 4.83% and 1393 MPa, and 4.77% and 1436 MPa, respectively. As expected, the Ta5 HESMA demonstrated better comprehensive performance. Its maximum recoverable strain and the corresponding compression strength were 9.4% and 2100 MPa, respectively, and the fracture strain was approximately 15%. The experimental results of the five newly prepared HESMAs show that it is feasible to find new HESMAs with good comprehensive performance by designing low C_v values. However, it should be noted that the C_v values were only one of the important factors. The solubility of the X-element and the precipitation of the secondary phase would certainly affect the comprehensive properties of the HESMAs, which need to be further studied.

4. Conclusions

Novel as-cast $(TiHfX)_{50}(NiCu)_{50}$ HESMAs with an excellent combination of superelasticity and mechanical properties were fabricated. The high strength and large recoverable strain make the high-entropy memory alloy have high output work. Coupled with its low cost and good stability, this material has great application potential in antiseismic and damping structures, medical devices, mechanical connections and so on. To the best of the authors' knowledge, such a large recoverable strain of 9.4% is the highest value among the reported polycrystalline Ti-Ni-based SMAs obtained by the melting method without any heat treatment. It is believed that the lower elastic modulus and lattice distortion strengthening effect of HEA contributed to the large recoverable strain characteristics

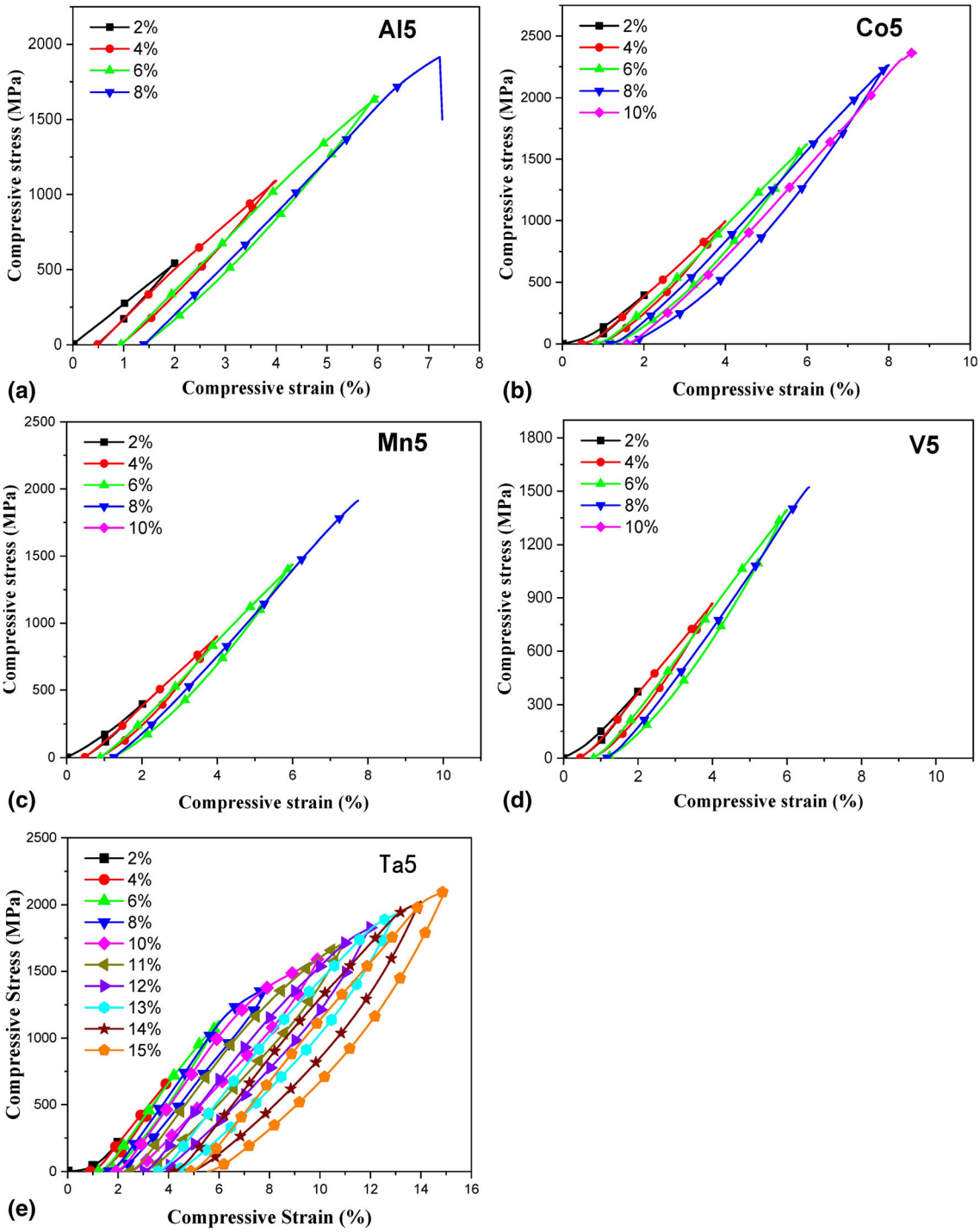

Fig. 7 The loading-unloading compression curves of Al5, Co5, Mn5, V5 and Ta5 HESMAs with increased prestrain

of HESMAs. The strategy of finding HESMAs with good comprehensive properties by designing low C_v values may provide useful guidelines in this field.

Acknowledgments

We acknowledge the financial supports from the Hubei provincial Department of Education (No. B2020024); the Opening Fund of Hubei Engineering Research Center for Graphite Additive Manufacturing Technology and Equipment (No. HRCGAM202104).

References

1. G.S. Firstov, T.A. Kosorukova, Y.N. Koval and V.V. Odnosum, High Entropy Shape Memory Alloys, *Mater. Today Proc.*, 2015, **2S**, p S499

2. J.W. Yeh, S.K. Chen, S.J. Lin, J.Y. Gan, T.S. Chin, T.T. Shun, C.H. Tsau and S.Y. Chang, Nanostructured High-Entropy Alloys with Multiple Principal Elements: Novel Alloy Design Concepts and Outcomes, *Adv. Eng. Mater.*, 2004, **6**(5), p 299–303
3. C.H. Chen, Y.J. Chen and J.J. Shen, Microstructure and Mechanical Properties of $(TiZrHf)_{50}(NiCoCu)_{50}$ High Entropy Alloys, *Met. Mater. Int.*, 2020, **26**, p 617
4. X.C Ye, Z.H. Cheng, C. Liu, X. Wu, L.E. Yu, M.Y. Liu, D. Fang, G.W Zhao, and B. Li, The Microstructure And Properties of $Fe_{55}Cr_{15}Ni_{(30-x)}Nb_x$ Eutectic High-Entropy Alloys, *Mater. Sci. Eng. A*, 2022, **844**, p 143026
5. T.A. Kosorukova, G. Gerstein, V.V. Odnosum, Y.N. Koval, H.J. Maier and G.S. Firstov, Microstructure Formation in Cast TiZrHfCoNiCu and CoNiCuAlGaIn High Entropy Shape Memory Alloys: A Comparison, *Materials.*, 2019, **12**, p 4227
6. G.S. Firstov, T.A. Kosorukova, Y.N. Koval and P.A. Verhovlyuk, Directions for High-Temperature Shape Memory Alloys' Improvement: Straight Way to High-Entropy Materials?, *Shap. Mem. Superelasticity.*, 2015, **1**, p 400
7. J. Yaacoub, W. Abuzaid, F. Brenne and H. Sehitoglu, Superelasticity of $(TiZrHf)_{50}Ni_{25}Co_{10}Cu_{15}$ High Entropy Shape Memory Alloy, *Scr. Mater.*, 2020, **186**, p 43–47
8. H.C. Lee, Y.J. Chen, and C.H. Chen, Effect of Solution Treatment on the Shape Memory Functions of $(TiZrHf)_{50}Ni_{25}Co_{10}Cu_{15}$ High Entropy Shape Memory Alloy., *Entropy*, 2019, **21**, p 1027
9. C.H. Chen and Y.J. Chen, Shape Memory Characteristics of $(TiZrHf)_{50}Ni_{25}Co_{10}Cu_{15}$ High Entropy Shape Memory Alloy, *Scr. Mater.*, 2019, **162**, p 185–189
10. S.H. Chang, P.T. Lin and C.W. Tsai, High-Temperature Martensitic Transformation of CuNiHfTiZr High-Entropy Alloys, *Sci. Rep.*, 2019, **9**, p 19598
11. S.H. Li, D.Y. Cong, Z. Chen, S.W. Li, C. Song, Y.X. Cao, Z.H. Nie and Y.D. Wang, A High-Entropy High-Temperature Shape Memory Alloy with Large and Complete Superelastic Recovery, *Mater. Res. Lett.*, 2021, **9**, p 263–269
12. S.H. Li, D.Y. Cong, X.M. Sun, Y. Zhang, Z. Chen, Z.H. Nie, R.G. Li, F.Q. Li, Y. Ren and Y.D. Wang, Wide-Temperature-Range Perfect Superelasticity and Giant Elastocaloric Effect in a High Entropy Alloy, *Mater. Res. Lett.*, 2019, **7**, p 482–498
13. D. Canadinc, W. Trehern, J. Ma, I. Karaman, F.P. Su and Z. Chaudhry, Ultra-High Temperature Multi-Component Shape Memory Alloys, *Scr. Mater.*, 2019, **158**, p 83–87
14. D. Piorunek, J. Frenzel, N. Jöns, C. Somsen and G. Eggeler, Chemical Complexity, Microstructure and Martensitic Transformation in High Entropy Shape Memory Alloys, *Intermetallics*, 2020, **122**, 106792
15. D. Piorunek, O. Oluwabi, J. Frenzel, A. Kostka, H.J. Maier, C. Somsen and G. Eggeler, Effect of Off-Stoichiometric Compositions on Microstructures and Phase Transformation Behavior in Ni-Cu-Pd-Ti-Zr-Hf High Entropy Shape MemoryAlloys, *J. Alloy. Compd.*, 2021, **857**, 157467
16. L. Wang, C. Fu, Y.D. Wu, R.G. Li, X.D. Hui and Y.D. Wang, Superelastic Effect in Ti-rich High Entropy Alloys Via Stress-Induced Martensitic Transformation, *Scr. Mater.*, 2019, **162**, p 112–117
17. J.J. Gao, P. Castany and T. Gloriant, Synthesis and Characterization of a New TiZrHfNbTaSn High-Entropy Alloy Exhibiting Superelastic Behavior, *Scr. Mater.*, 2021, **198**, 113824
18. N. Hashimoto, Y.A. Zain, A. Yamamoto, T. Koyano, H.Y. Kim and S. Miyazaki, Ovel Beta-Type High Entropy Shape Memory Alloys with Low Magnetic Susceptibility and High Biocompatibility, *Mater. Lett.*, 2021, **287**, 129286
19. C.H. Chen, N.H. Lu, J.J. Shen and Y.J. Chen, Strain Glass and Stress-Induced Martensitic Transformation Characteristics of $Ti_{40}Zr_{10}Ni_{40-}Co_5Cu_5$ Multi-Principal Element Alloy, *Scr. Mater.*, 2020, **186**, p 127–131
20. R.E. Rajeshwar, K. Margarita, T. Mikhail, S. Nikita and Z. Sergey, Exceptionally High Strain-Hardening and Ductility due to Transformation Induced Plasticity Effect in Ti-rich High-Entropy Alloys, *Sci. Rep.*, 2020, **10**, p 13293
21. G.W. Zhao, J. Chen, C. Ding, D. Fang, C.H. Huang and X.C. Ye, Effect of Yttrium on the Microstructure, Phase Transformation and Superelasticity of a Ti-Ni-Cu Shape Memory Alloy, *Vacuum*, 2020, **177**, 109381
22. G.W. Zhao, J. Chen, Y.S. Ye, C.H. Huang and X.C. Ye, Effect of Mo on the Microstructure and Superelasticity of Ti-Ni-Cu Shape Memory Alloys, *JMEPEG*, 2021, **30**, p 617
23. S.H. Chang, W.P. Kao, K.Y. Hsiao, J.W. Yeh, M.Y. Lu, and C.W. Tsai, High-Temperature Shape Memory Properties of $Cu_{15}Ni_{35-}Ti_{25}Hf_{12.5}Zr12.5$ High-Entropy Alloy, *J. Mater. Res. Technol.*, 2021, **14**, p 1235-1242
24. J.S. Kim, Y.J. Kim, W.C. Kim, W.T. Kim and D.H. Kim, Enhancement in Strength and Superelastic Cyclic Durability by Addition of Si in Ni-Ti-Cu-Zr Alloy, *Intermetallics*, 2020, **124**, 106867
25. K.S. Sun, X.Y. Yi, B. Sun, W.H. Gao, H.Z. Wang, X.L. Meng, W. Cai and L.C. Zhao, The Effect of Hf on the Microstructure, Transformation Behaviors and the Mechanical Properties of Ti-Ni-Cu Shape Memory Alloys, *J. Alloys. Compd.*, 2019, **772**, p 603–611
26. G.C. Wang, K.P. Hu, Y.X. Tong, B. Tian, F. Chen, L. Li, Y.F. Zheng and Z.Y. Gao, Influence of Nb Content on Martensitic Transformation and Mechanical Properties of TiNiCuNb Shape Memory Alloys, *Intermetallics*, 2016, **72**, p 30–35
27. J. Li, X.Y. Yi, K.S. Sun, B. Sun, W.H. Gao, H.Z. Wang, X.L. Meng and W.L. Song, The Effect of Zr on the Transformation Behaviors, Microstructure and the Mechanical Properties of Ti-Ni-Cu Shape Memory Alloys, *J. Alloys. Compd.*, 2018, **747**, p 348–353
28. W. Abuzaid and H. Sehitoglu, Superelasticity and Functional Fatigue of Single Crystalline FeNiCoAlTi Iron-Based Shape Memory Alloy, *Mater. Design.*, 2018, **160**, p 642–651
29. L.L. Pavón, E.L. Cuellar, S.V. Hernandez, I.E. Moreno-Cortez, H.Y. Kim and S. Miyazaki, Effect of Heat Treatment Condition on Microstructure and Superelastic Properties of Ti24Zr10Nb2Sn, *J. Alloys. Compd.*, 2019, **782**, p 893–898
30. K. Endoh, M. Tahara, T. Inamura and H. Hosoda, Effect of Sn and Zr Content on Superelastic Properties of Ti-Mo-Sn-Zr Biomedical Alloys, *Mater. Sci. Eng. A*, 2017, **704**, p 72–76
31. S.Y. Yang, F. Zhang, J.L. Wu, Y. Lu, Z. Shi, C.P. Wang and X.Y. Liu, Superelasticity and shape memory effect in Cu-Al-Mn-V shape memory alloys, *Mater. Design.*, 2017, **115**, p 17–25
32. H.G. Armaki, A.C. Leff, M.L. Taheri, J. Dahal, M. Kamarajugadda and K.S. Kumar, Cyclic Compression Response of Micropillars Extracted from Textured Nanocrystalline NiTi Thin-Walled Tubes, *Acta Mater.*, 2017, **136**, p 134–147
33. P. Hua, K.J. Chu, F.Z. Ren and Q.P. Sun, Cyclic Phase Transformation Behavior of Nanocrystalline NiTi at Microscale, *Acta Mater.*, 2020, **185**, p 507–517
34. X.R. Chen, F. Zhang, M.Y. Chi, S.Y. Yang, C.P. Wang, X.J. Liu and S.S. Zheng, Microstructure, Superelasticity and Shape Memory Effect by Stress-Induced Martensite Stabilization in Cu-Al-Mn-Ti Shape Memory Alloys, *Mater. Sci. Eng. A*, 2018, **236–237**, p 10–17
35. S.Y. Yang, M.Y. Chi, J.X. Zhang, K.X. Zhang, X.Y. Liu, C.P. Wang and X.J. Liu, Shape Memory Effect Promoted Through Martensite Stabilization Induced by the Precipitates in Cu-Al-Mn-Fe Alloys, *Mater. Sci. Eng. A*, 2019, **739**, p 455–462
36. J. Chen, S.W. Zhang, Y.H. Zhang, J. Zhang, Y.H. Wen, Q. Yang, S.K. Huang and X.B. Wang, A Study on the Cold Workability and Shape Memory Effect of NiTiHf-Nb Eutectic High-Temperature Shape Memory Alloy, *Intermetallics*, 2020, **127**, 106982
37. H. Chen, F. Xiao, X. Liang, Z.X. Li, X.J Jin, and T. Fukuda, Stable and Large Superelasticity and Elastocaloric Effect in Nanocrystalline Ti-44Ni-5Cu-1Al (at%) Alloy, *Acta Mater.*, 2018, **158**, p 330-339
38. H.E. Karaca, E. Acar, B. Basaran, R.D. Noebe, G. Bigelow, A. Garg, F. Yang, M.J. Millsd and Y.I. Chumlyakov, Effects of Aging on (Ref 1 1 1) Oriented NiTiHfPd Single Crystals Under Compression, *Scr. Mater.*, 2012, **67**, p 728–731
39. X.Y. Yi, G.J. Shen, X.L. Meng, H.Z. Wan, Z.Y. Gao, W. Cai and L.C. Zhao, The Higher Compressive Strength $(TiB+La_2O_3)$/Ti–Ni Shape Memory Alloy Composite with the Larger Recoverable Strain, *Compos. Commun.*, 2021, **23**, 100583
40. X.Y. Yi, X.L. Meng, W. Cai and L.C. Zhao, Larger Strain Recovery Characteristics of Ti-Ni-Hf Shape Memory Alloy Composite Under Compression, *Scr. Mater.*, 2018, **153**, p 90–93
41. Y. Zhao, F. Ming, N. Jia, J.H. Chen, S.B. Ren, W. Xu, X.H. Qu, High-Strength Superelastic As-Cast $Ni_{50.9}Ti_{49.1}$-TiB_2 in-situ Composites, *Mater. Sci. Eng. A*, 2021, **818**, p 141451
42. H. Sehitoglu, Y. Wu, L. Patriarca, G. Li, A. Ojha, S. Zhang, Y. Chumlyakov and M. Nishida, Superelasticity and Shape Memory

Behavior of NiTiHf Alloys, *Shap. Mem. Superelast.*, 2017, **3**, p 168–187
43. S.M. Saghaian, H.E. Karaca, H. Tobe, A.S. Turabi, S. Saedi, S.E. Saghaian, Y.I. Chumlyakov and R.D. Noebe, High Strength NiTiHf Shape Memory Alloys with Tailorable Properties, *Acta Mater.*, 2017, **134**, p 211–220
44. X.Y. Yi, K.S. Sun, W.H. Gao, X.L. Meng, W. Cai and L.C. Zhao, Martensitic Transformation and Mechanical Properties of Ti-Ni-Hf high Temperature Shape Memory Alloy with Network Structure Second Particles, *J. Alloys. Compd.*, 2018, **735**, p 1219–1226
45. S.S. Liu, C.Q. Xia, T. Yang, Z.D. Yang, N. Liu and Q. Li, High Strength and Superior Corrosion Resistance of the Ti-Ni-Cu-Zr Crystal/Glassy Alloys with Superelasticity, *Mater. Lett.*, 2020, **260**, 126938
46. X.Y. Yi, W.H. Gao, X.L. Meng, Z.Y. Gao, W. Cai and L.C. Zhao, Martensitic Transformation Behaviors and Mechanical Properties of $(Ti_{36}Ni_{49}Hf_{15})_{100-x}Yx$ High Temperature Shape Memory Alloys, *J. Alloys. Compd.*, 2017, **705**, p 98–104
47. M. Zarinejad and Y. Liu, Dependence of Transformation Temperatures of NiTi-based Shape-Memory Alloys on the Number and Concentration of Valence Electrons, *Adv. Funct. Mater.*, 2008, **18**, p 2789–2794
48. X.L. Han, K.K. Song, L.M. Zhang, H. Xing, B. Sarac, F. Spieckermann, T. Maity, M. Mühlbacher, L. Wang, I. Kaban and J. Eckert, Microstructures Martensitic Transformation, and Mechanical Behavior of Rapidly Solidified Ti-Ni-Hf and Ti-Ni-Si Shape Memory Alloys, *JMEPEG*, 2018, **27**, p 1005–1015
49. J.J. Gilman, R.W. Cumberland and R.B. Kaner, Design of Hard Crystals, *Int. J. Refract. Met. Hard Mater.*, 2006, **24**, p 1–5
50. W.C. Kim, K.R. Lim, W.T. Kim, E.S. Park, and D.H. Kim, Recent Advances in Multicomponent NiTi-based Shape Memory Alloy Using Metallic Glass as a Precursor, *Prog. Mater. Sci.*, 2021, p 100855